instruments

MDPI

Article

Calibration of a Capacitive Coupled Ring Resonator for Non-Invasive Measurement of Wood Moisture Content

Livio D'Alvia [1,2,*], Ludovica Apa [2], Emanuele Rizzuto [2], Erika Pittella [3,*] and Zaccaria Del Prete [2]

[1] Department of Well-Being, Health and Environmental Sustainability (BeSSA), Sapienza Università di Roma, Via della Fontanelle, 02100 Rieti, Italy
[2] Department of Mechanical and Aerospace Engineering (DIMA), Sapienza Università di Roma, Via Eudossiana 18, 00184 Rome, Italy; ludovica.apa@uniroma1.it (L.A.); emanuele.rizzuto@uniroma1.it (E.R.); zaccaria.delprete@uniroma1.it (Z.D.P.)
[3] Department of Information Engineering, Electronics and Telecommunications (DIET), Sapienza Università di Roma, Via Eudossiana 18, 00184 Rome, Italy
* Correspondence: livio.dalvia@uniroma1.it (L.D.); erika.pittella@uniroma1.it (E.P.)

Abstract

The accurate and non-invasive measurement of moisture content in wood is essential for the preservation of historical and artistic artifacts. This study presents the calibration of a planar Microwave Planar Capacitive Coupled Ring Resonator (MPCCRR) designed to indirectly and non-destructively assess the water content in wood samples. The method relies on analyzing shifts in the resonant frequencies and variations in the transmission parameter |S21| resulting from changes in the material's dielectric permittivity. After preliminary characterization via parametric simulations (εr = 1–10) and validation with low-permittivity reference materials, the sensor was tested on three wood species (poplar, fir, beech), including measurements at two sensor positions and with different grain orientations. The results demonstrate a monotonic, repeatable response to increasing moisture content with frequency shifts up to ≈220 MHz and normalized sensitivities ranging from 3 to 9 MHz/% water content, depending on species and measurement position. Position 2 showed the greatest sensitivity due to stronger field–sample interaction, while Position 1 provided a quasi-isotropic response with excellent repeatability. Linear regression analyses revealed good correlations between the frequency shifts and the gravimetric water content ($R^2 \geq 0.85$). The MPCCRR sensor therefore proves to be a promising tool for the non-invasive monitoring of wood moisture, which is particularly suitable for the low-moisture range encountered in cultural heritage conservation, with an estimated moisture uncertainty of 0.12–0.35% under controlled laboratory conditions.

Keywords: dielectric measurements; moisture measurement; split ring resonator; microwave sensors; wood

Check for updates

Academic Editor: Antonio Ereditato

Received: 9 December 2025
Revised: 22 January 2026
Accepted: 30 January 2026
Published: 5 February 2026

Copyright: © 2026 by the authors. Licensee MDPI, Basel, Switzerland. This article is an open access article distributed under the terms and conditions of the Creative Commons Attribution (CC BY) license.

1. Introduction

In the field of cultural heritage—encompassing historical buildings, sculptures, furniture, musical instruments, and artworks—wood is a fundamental material [1]. However, it is particularly susceptible to moisture-related damage, which can cause dimensional changes, warping, cracking, and, in severe cases, structural failure. Elevated moisture levels can also promote the growth of fungi, microorganisms, and mold, accelerating degradation and compromising both the aesthetic value and structural integrity of the artifacts [2]. For

these reasons, the accurate and non-destructive measurement of wood moisture content is essential for its preservation [3–7].

Electrical techniques (ETs) play a vital role in assessing wood moisture in cultural heritage objects without damaging the artifacts. ET can be adapted to various object types, materials, and geometries, making them versatile tools capable of probing moisture content across a wide range of heritage materials [8,9]. A key advantage of microwave-based techniques is their non-intrusive nature: they minimize or eliminate physical contact with the object under investigation, ensuring the artifact remains unaltered during the measurement process. This makes them particularly suitable for conservation purposes. Today, various ET methods are routinely employed due to their versatility and low intrusiveness [10], including electrical conductance [11], electrical impedance [12], or microwave-based methods [13].

Recently, resonance-based microwave techniques have gained increasing attention for moisture measurement in heritage materials such as stone [14] and wood [15]. These methods exploit the dependence of dielectric properties on moisture content and analyze resonance characteristics—including resonance frequency (fr), scattering parameters ($|Sij|$), and quality factor (Q). Such techniques offer several advantages over conventional approaches, including non-invasiveness, soft-contact operation, and higher sensitivity and precision [16].

Different resonator configurations have been proposed, such as planar structures, cavity resonators, open-ended coaxial probes, and ring resonators, which are all designed to operate at specific resonant frequencies. These frequencies correspond to points of maximum electromagnetic energy absorption by the material [17]. As microwaves propagate through a substance, they undergo absorption and phase-shift phenomena that depend on the material's permittivity (ε), which reflects the polarization of both wood components and water molecules under the applied electric field. The strong contrast between the high permittivity of water ($\varepsilon r \approx 78$) and that of dry wood ($\varepsilon r \approx 2$) makes microwave resonance-based techniques particularly suitable for moisture detection [17,18].

Several configurations of planar resonators have recently been proposed [19]; for example, Ekmekci et al. [20] analyzed double-sided resonator structures for humidity and gas sensing, Xie et al. [21] developed a square split-ring resonator probe for detecting subsurface wood defects and moisture, and Pittella et al. [22] introduced a split-ring resonator network for water content assessment.

In the specific context of wood and cultural heritage materials, planar microwave resonator-based sensors have been investigated for moisture assessment due to their non-invasive nature and sensitivity to dielectric variations. Previous studies have explored resonant probes and planar structures for wood moisture monitoring under controlled laboratory conditions, highlighting both their potential and their sensitivity to material anisotropy and measurement configuration [23–25]. However, most existing works primarily focus on sensor design or sensitivity enhancement with limited emphasis on experimental calibration strategies, uncertainty quantification, and practical measurement guidelines for heterogeneous heritage materials.

In this study, which extends the numerical feasibility analysis presented in D'Alvia et al. [26], we report the first experimental calibration and validation of a Microwave Planar Capacitive Coupled Ring Resonator (MPCCRR) for the non-invasive assessment of water content in wood samples. In particular [26], two alternative resonator configurations (capacitive and inductive coupling) were comparatively investigated exclusively through electromagnetic simulations without experimental measurements or calibration. Based on those results, the present work deliberately focuses on the capacitive configuration and extends it to real measurements on materials.

Specifically, in this paper, the sensor is experimentally tested on three wood species—poplar, fir, and beech—including fir samples with different grain orientations over more than eight moisture levels for each sample. The numerical simulations previously reported in [26] are briefly recalled for methodological completeness and to support the interpretation of the experimental results, while the core contribution of this paper lies in the experimental characterization, calibration framework, and uncertainty analysis.

The remainder of the manuscript is organized as follows: Section 2 describes the sensor design, wood samples, and experimental setup; Section 3 presents the calibration methodology and uncertainty analysis; Section 4 reports the experimental results and discussion; finally, Section 5 draws conclusions and outlines future work.

2. Materials and Methods

2.1. Sensor Design

A coupled microwave resonator structure is obtained by interconnecting two or more ring-shaped elements, forming a single resonant system characterized by multiple resonant modes and enhanced electromagnetic field confinement. The coupling strength between the rings can be tailored by modifying parameters such as ring separation, length, orientation, or overall geometry, thereby enabling control over resonance frequencies and field distribution. Compared to conventional resonator configurations—such as cavity resonators or planar patch resonators—the proposed architecture features a compact planar geometry that facilitates integration into measurement setups for non-invasive sensing. The reduced footprint allows reliable measurements on small samples while improving positioning repeatability, which is particularly relevant for cultural heritage applications.

The proposed sensor consists of planar microstrip ring resonators arranged in a capacitive-coupling configuration, as originally introduced by Zarifi et al. [27] and later adapted by D'Alvia et al. [26]. The sensor layout is shown in Figure 1a. In this design, the inner rings are electrically interconnected and excited by inductive coupling between the feed lines and the outer perimeter of the ring. Figure 1a also reports the dimensional parameters of the structure and the sample positioning areas.

According to [16], the resonance frequency of each ring can be approximated as Equation (1):

$$f_r = \frac{c}{2L_{eff}\sqrt{\varepsilon_{eff}}} \quad (1)$$

where c is the speed of light, L_{eff} is the effective length of the ring, and ε_{eff} is the effective permittivity of the resonator. The value of ε_{eff} depends on both the surrounding air and the material placed in contact with the sensing region, which perturbs the local electromagnetic field distribution.

The proposed MPCCRR exhibits a dual-resonance response with a high-frequency mode at f_h = 2.72 GHz, a low-frequency mode at f_l = 2.578 GHz, and a frequency separation Δ = 0.150 GHz. The simulated insertion loss for ε = 1 (air) is shown in Figure 1b, where the two resonance peaks are clearly visible.

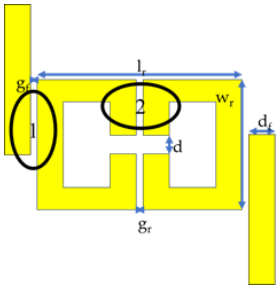
2.2. Preliminary Sensor Characterization

The sensor design and preliminary electromagnetic analysis were performed using CST Studio Suite. A wood sample with dimensions 22 mm × 11 mm × 8 mm was also modeled to evaluate the sensor response under different dielectric conditions. The relative permittivity of the sample was systematically varied from ε_r = 1 (air) to ε_r = 10, simulating the increasing moisture content levels typically encountered in wood.

To assess the influence of sample positioning on the resonant behavior, the model was evaluated in two measurement configurations: P1: sample placed above the feed

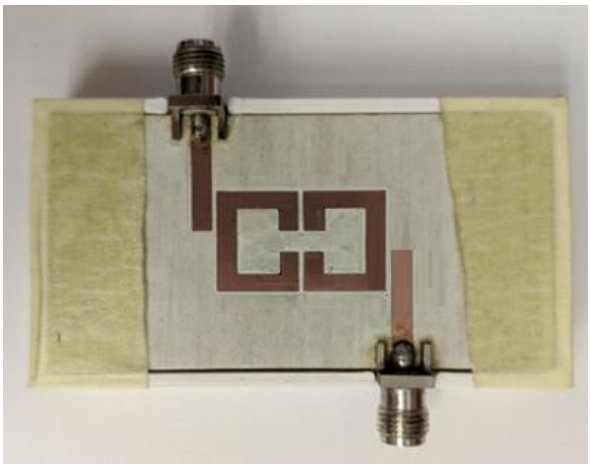
gaps (g_f) and P2: sample placed above the ring gap (g_r). These positions, shown in Figure 1a, expose the sample to different regions of the resonator's electromagnetic field. This configuration enables a comparative analysis of how the sample location affects the resonant characteristics—specifically, shifts in resonance frequencies—and the sensor's capability to discriminate moisture-induced permittivity variations.

Additionally, simulations were performed varying the sample thickness from 1 to 16 mm to investigate the effect of sample thickness on the sensor response. This analysis allowed the identification of a thickness threshold beyond which the resonant frequency shift becomes weakly dependent on further increases in sample height.

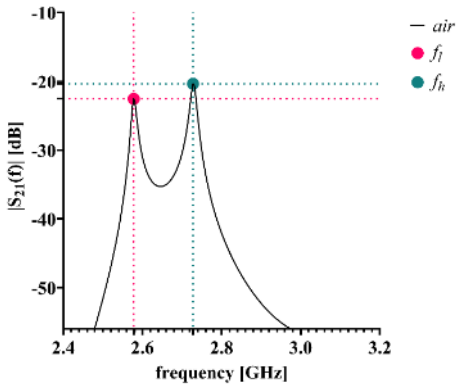


Parameter	Symbol	Dimension (mm)
Feed line depth	d_f	2.8
Ring width	w_r	14
Ring length	l_r	21
Ring gap	gr	0.6
Split distance	d	2
Feed gap	g_f	0.8

(**a**)



(**b**)



(**c**)

Figure 1. Microwave Planar Capacitive Coupled Ring Resonator (MPCCRR) design and features: (**a**) MPCCRR design with highlighted dimensional parameters and the sample positioning adapted from [23], (**b**) real MPCCRR, and (**c**) MPCCRR computed insertion loss for $\varepsilon = 1$ (air) with the two peaks at f_l and f_h highlighted.

2.3. Wood Sample Dimensions

For this study, one wood sample was selected from each of three species: poplar, fir, and beech. All samples were prepared with dimensions of 22 mm × 11 mm × 8 mm. The selected dimensions ensured compatibility with both simulation and experimental configurations while maintaining the representative bulk behavior of the material.

To investigate the influence of grain orientation on moisture measurements, two additional fir samples were included: one with the grain direction parallel to the plane of the MPCCRR probe and the other perpendicular to it. Before the measurements, all samples were carefully cut to uniform dimensions to ensure consistency throughout the experimental procedure. As in the simulation step, each wood sample was positioned

in P1 and P2 during testing. The initial mass of every specimen was measured using an electronic balance and recorded for subsequent calculation of water content.

2.4. Experimental Setup and Measurement Procedure

In this study, the wood moisture content was estimated by analyzing shifts in the resonance frequency f_r induced by changes in the dielectric properties of the material. Variations in the dielectric properties of the material were correlated with changes in the transmission scattering parameter $|S_{21}(f)|$ occurring when the radiating probe lay on the material surface; according to theoretical considerations, the variation in the resonance frequency f_r of the probe was found to be associated with the water content in the tested material [28].

As a preliminary assessment, the sensor's capability to distinguish small variations in relative permittivity ε_r was evaluated using four reference plastic materials with known dielectric constants in the range $\varepsilon_r \in [1.5, 3.0]$ at frequencies between 1 and 3 GHz [29]. Specifically, these materials are outlined below:

- LD-PVC (Low-Density PolyVinylChloride) with ε_r = 1.62;
- PTFE (PolyTetraFluoroEthylene) with ε_r = 2.06;
- PMMA (PolyMethylMethAcrylate) with ε_r = 2.60;
- PC (PolyCarbonate) with ε_r = 2.82.

All samples had the same dimensions as the wood specimens except for the LD-PVC, which was 2 mm thinner.

For wood measurements, each dried sample was first weighed using a 10 mg resolution electronic balance [30], and the corresponding sensor response was acquired with a vector network analyzer (VNA) [31]. The sample was then immersed in deionized water until three consecutive measurements showed no further change (5 min). The sample was removed, and the surface water was blotted using laboratory tissue. The sensor response was first recorded at the maximum moisture level, and subsequent measurements were taken at six intermediate moisture levels as the sample gradually dried, blotting with laboratory tissue before each measurement to avoid a surface water layer.

The gravimetric water content (θ%) was calculated according to Equation (2):

$$\theta(\%) = \frac{W_i - W_{dry}}{V \times \rho}\% \tag{2}$$

where W_i is the mass of the moist specimen, W_{dry} is the dried sample's mass, V is the sample volume and ρ is the density of water. The steps of the measurement procedure are similar to those detailed in [15].

All measurements were performed using a PicoVNA 108, operating in the 300 kHz–8.5 GHz range [30], at the controlled environmental temperature of (24 ± 2) °C.

2.5. Post-Processing Analysis

The resonance frequencies and the frequency spacing Δf between the two peaks were determined from the transmission loss. Regression lines were then fitted to relate the measured resonance frequencies to the corresponding water content levels of the wood samples. This procedure highlights the trends and correlations between the material permittivity and the associated resonance frequencies. Such information is essential for constructing calibration models that enable an accurate estimation of water content from the measured resonance frequencies once the physical sensor is implemented.

The normalized sensitivity S (%) of the sensor was computed for both resonance bands and for each measurement position according to the following equation:

$$S(\%) = \left| \frac{(f_{air} - f_i)}{f_i(\varepsilon - 1)} \right| \% \quad (3)$$

where f_{air} is the resonance frequency when the sensors are unloaded (ε = 1), f_i is the frequency when the i-th sample under test is placed on the top of the sensors, and ε is the permittivity value of the material under test. This post-processing procedure forms the basis for the calibration models discussed in Section 3, enabling a quantitative estimation of moisture content from the measured resonance frequency shifts.

3. Uncertainty Analysis and Calibration Approach

3.1. Uncertainty Analysis

An instrumental uncertainty assessment was carried out to quantify the precision limits associated with the measurement chain. This analysis considers only a priori uncertainties originating from the instrumentation and acquisition procedures and does not include uncertainties arising from material variability or calibration model assumptions.

1. Electronic balance uncertainty

The wood mass was measured using a 10 mg resolution electronic balance.
For typical samples (≈2–3 g), the relative uncertainty of the dry mass is below:

$$U_m \approx \frac{0.01\ \text{g}}{2.00\ \text{g}} \approx 0.5\% \quad (4)$$

This propagates directly into the gravimetric water content (Equation (2)), resulting in a conservative uncertainty of ±0.05–0.10% in θ for low-moisture conditions.

2. VNA frequency uncertainty

Frequency acquisition was performed with a PicoVNA 108. According to the manufacturer specifications, the frequency accuracy is outlined below:

$$U_f^{VNA} = \pm(0.2\%_{\text{span}} + 1\ \text{MHz}) \quad (5)$$

Considering the narrow sweep windows around the resonance peaks (≈100 MHz), the dominant term is ±1 MHz.

3. Peak extraction repeatability

Resonance frequencies were extracted using an automated algorithm based on interpolation of the maximum of $|S_{21}(f)|$. Five repeated measurements on a stable reference sample provided a peak detection repeatability of

$$U_f^{fit} \approx \pm 0.5\ \text{MHz} \quad (6)$$

4. Combined instrumental frequency uncertainty

Assuming independent and uncorrelated contributions, the total instrumental uncertainty on the resonant frequency measurement is

$$U_f = \sqrt{\left(U_f^{(VNA)}\right)^2 + \left(U_f^{(fit)}\right)^2} \quad (7)$$

$$U_f = \sqrt{(1\ \text{MHz})^2 + (0.5\ \text{MHz})^2} = 1.1\ \text{MHz} \quad (8)$$

this value represents the minimum resolvable frequency shift imposed by the instrumentation alone independent of the material under test or the adopted calibration model. Therefore, it can be regarded as a lower bound estimate of the achievable uncertainty under controlled experimental conditions.

3.2. Calibration Approach

Supposing a linear regression analysis, the gravimetric moisture content θ (%) can be estimated from the shift of the low and high frequency mode using

$$\theta = \alpha \cdot (f_l - f_{l,0}) + \beta \cdot (f_h - f_{h,0}) + \gamma \quad (9)$$

where $f_{l,h}$ = measured low/high-frequency resonance, $f_{l,h,0}$ = low/high resonance of the dry sample; α and β = sensitivity coefficient (MHz/%) and representing the change in moisture content per MHz frequency shift for the low- and high-frequency modes, respectively; γ = offset (typically ≈ 0), introduced to account for baseline normalization.

The introduction of the α and β coefficients allows accounting for both bulk interactions and material heterogeneities. The α coefficient, representing the sensitivity of the low-frequency mode to changes in moisture content, allows quantifying the expected change in θ per MHz of frequency shift and generally reflects the bulk interaction of the sample with the electromagnetic field. The β coefficient, representing the sensitivity of the high-frequency mode, captures additional contributions from localized field perturbations and material heterogeneities.

4. Results and Discussion

4.1. Preliminary Sensor Characterization Results

Table 1 shows the resonance frequencies (f_l and f_h) and their difference (Δf_l) for Position 1 across varying permittivity (ε) values from 1 to 10. For this configuration, both resonance frequencies remain nearly constant across all permittivity values, showing only minor fluctuations within the expected numerical noise. Consequently, Δf also remains stable—between 0.135 and 0.165 GHz—indicating that the response of the resonant structure in Position 1 is only weakly influenced by changes in the material permittivity. This limited dispersion suggests a lower sensitivity of this measurement point to variations in dielectric properties.

Table 1. Low and high-resonance frequencies and their difference for P1.

ε	f_l (GHz)	f_h (GHz)	Δf (GHz)
1	2.578	2.728	0.150
2	2.578	2.731	0.153
3	2.572	2.719	0.147
4	2.568	2.731	0.153
5	2.563	2.710	0.147
6	2.566	2.725	0.159
7	2.575	2.710	0.135
8	2.569	2.710	0.141
9	2.557	2.710	0.153
10	2.554	2.719	0.165

Table 2 summarizes the same parameters for Position 2. In this case, both f_l and f_h exhibit a clear decreasing trend as ε increases from 1 to 10. In contrast to Position 1, the separation between the two resonance frequencies widens progressively with Δf increasing from 0.150 GHz (ε = 1) to 0.303 GHz (ε = 10). This monotonic expansion reflects

a stronger interaction between the sample and the electromagnetic field at the ring gap region, indicating that Position 2 is substantially more sensitive to variations in permittivity.

Table 2. Low and high-resonance frequencies and their difference for P2.

ε	f_l (GHz)	f_h (GHz)	$\Delta f_{h\text{-}l}$ (GHz)
1	2.578	2.728	0.150
2	2.536	2.701	0.165
3	2.488	2.683	0.195
4	2.416	2.641	0.225
5	2.368	2.629	0.261
6	2.392	2.611	0.219
7	2.368	2.599	0.231
8	2.314	2.593	0.279
9	2.290	2.581	0.291
10	2.260	2.563	0.303

A comparison of the two configurations confirms that Position 2 provides a more pronounced and systematic frequency shift with respect to changes in ε, whereas Position 1 exhibits a much weaker response.

Normalized sensitivities computed according to Equation (3) are reported in Table 3. If Position 2 shows slightly higher sensitivities than Position 1 for f_l, f_h, and Δf at low permittivity values ($\varepsilon \geq 2$), Position 1 maintains a nearly constant Δf sensitivity of approximately 1% across all permittivity levels.

Table 3. Normalized sensitivity for the two frequency bands and the application point.

ε	P1			P2		
	S (%) f_l	S (%) f_h	S (%) Δf	S (%) f_l	S (%) f_h	S (%) Δf
2	0.00%	0.11%	2%	1.66%	1.00%	9%
3	0.12%	0.17%	1%	1.81%	0.84%	12%
4	0.00%	0.04%	1%	2.24%	1.10%	11%
5	0.15%	0.17%	1%	2.22%	0.94%	11%
6	0.09%	0.02%	1%	1.56%	0.90%	6%
7	0.02%	0.11%	2%	1.48%	0.83%	6%
8	0.05%	0.09%	1%	1.63%	0.74%	7%
9	0.10%	0.08%	0%	1.57%	0.71%	6%
10	0.10%	0.04%	1%	1.56%	0.72%	6%

The results obtained for configurations P1 and P2 of f_l and f_h as a function of the sample thickness 1 mm $\leq$ t $\leq$ 16 mm are summarized in Table 4

In both cases, both resonance frequencies show a clear dependence on the sample height for small values of h with a more pronounced variation observed below approximately 4 mm. To better interpret this behavior, the data were fitted using an exponential interpolating function of the form

$$y = p + (y_0 - p) \cdot e^{-k \cdot x} \tag{10}$$

where y represents the resonance frequency, x is the sample height, y_0 is the y value when x is zero, p is the y value at infinite and k is the rate constant. The interpolation highlights the presence of a plateau region occurring at a sample thickness of approximately 4 mm and above, beyond which further increases in thickness produce only minor variations in both f_l and f_h, as shown in Figure 2. This indicates that for both configurations, the sensor response becomes weakly dependent on the sample height once a critical thickness

is exceeded, suggesting that the electromagnetic field interaction is effectively saturated within this distance from the resonator.

Table 4. Resonance frequencies (f_l and f_h) as a function of sample thickness t for both configurations.

t (mm)	P1		P2	
	f_l (GHz)	f_h (GHz)	f_l (GHz)	f_h (GHz)
1	2.612	2.748	2.614	2.764
2	2.603	2.737	2.602	2.762
3	2.596	2.726	2.591	2.747
4	2.579	2.714	2.600	2.740
5	2.566	2.714	2.591	2.722
6	2.575	2.720	2.587	2.723
7	2.569	2.723	2.583	2.725
8	2.579	2.723	2.583	2.725
9	2.568	2.702	2.596	2.724
10	2.593	2.725	2.601	2.730
11	2.580	2.719	2.593	2.723
12	2.589	2.726	2.590	2.722
13	2.589	2.730	2.594	2.725
14	2.580	2.714	2.584	2.724
15	2.581	2.714	2.592	2.721
16	2.580	2.713	2.594	2.725

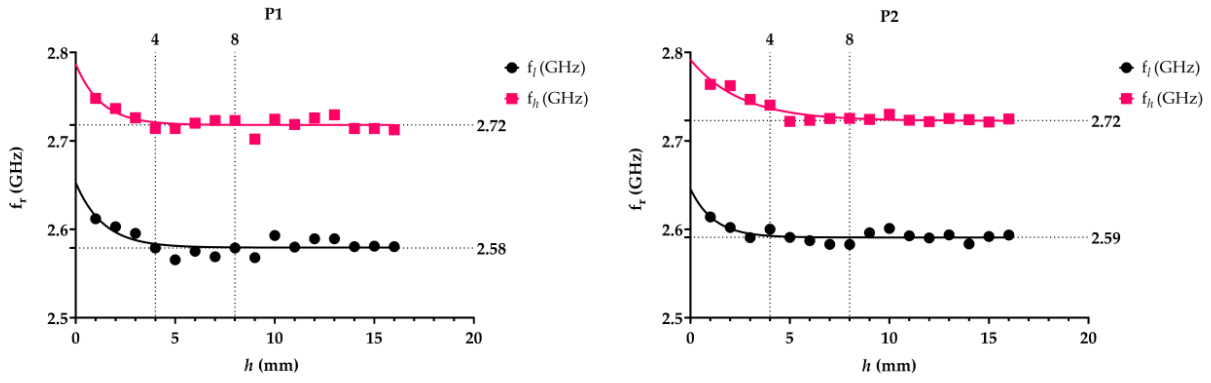


Figure 2. Resonance frequencies (f_l and f_h) as a function of sample thickness t for (**a**) configuration 1 and (**b**) configuration 2 with the plateau and the wood sample thickness highlighted.

4.2. Calibration Results

Table 5 reports the resonance frequencies (f_l and f_h) and the corresponding Δf for Position 1 and Position 2 when four reference plastic materials with known permittivity values are placed on the sensor. The measured transmission loss traces for these materials are shown in Figure 3a (Position 1) and Figure 3b (Position 2).

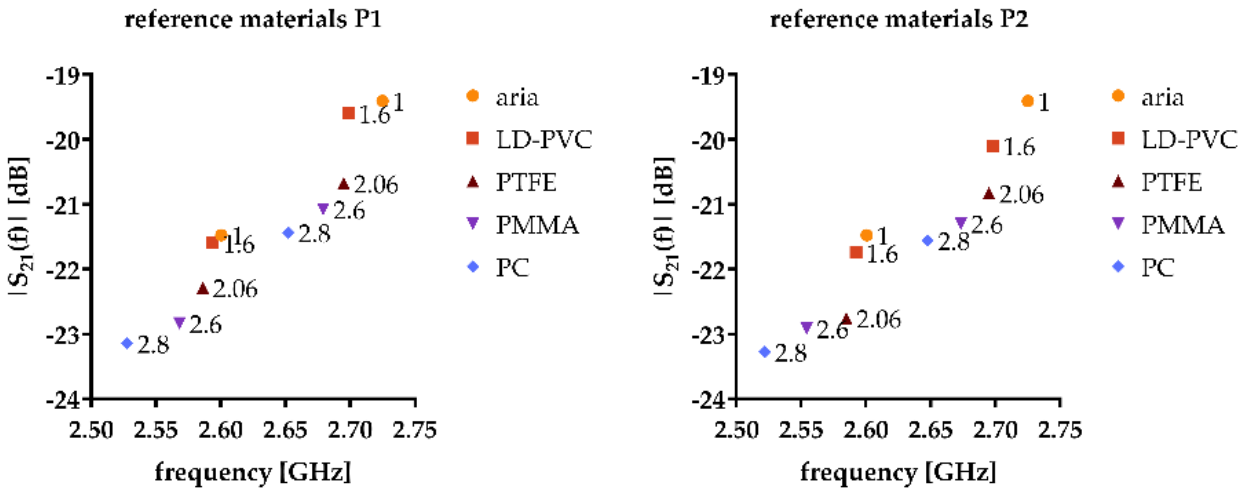
Although the four materials exhibit close permittivity values (ε = 1.6–2.8), the sensor can discriminate them based on their frequency response. In Position 1 (Figure 2a), the variations in both f_l and f_h are relatively small, and Δf remains almost constant across the materials. Nevertheless, the transmission coefficient $|S21|$ shows distinct amplitude differences for each material, enabling clear identification based on dielectric properties.

In Position 2 (Figure 2b), the frequency response is more sensitive to permittivity variations: both f_l and f_h show larger downward shifts as ε increases, and Δf exhibits a more pronounced spread across the four materials. This confirms that Position 2 offers improved sensitivity to dielectric variations, whereas Position 1 provides better contrast in the transmission magnitude. Taken together, the two measurement points complement

each other: Position 1 enhances material discrimination through |S21| magnitude differences, while Position 2 maximizes the detection of permittivity-induced frequency shifts (Figure 2a,b). An observation concerns the LD-PVC sample. Despite its nominal ε = 1.6, its measured response resembles that of a material with ε > 2, as reported in Tables 2 and 3. This deviation is explained by its reduced thickness (2 mm thinner than the other samples), suggesting how the variations in geometry can influence the measured resonance frequencies. This highlights the need for standardized calibration protocols when dealing with heterogeneous or irregular samples.

Table 5. Low and high-resonance frequencies for well-known materials for P1 and P2.

Pos	Material	ε	f(l, h) (GHz)	Δ*f* (GHz)
-	Air	1.0	2.601~2.725	0.124
1	LD-PVC	1.6	2.594~2.699	0.105
	PTFE	2.06	2.586~2.695	0.109
	PMMA	2.6	2.568~2.679	0.111
	PC	2.8	2.528~2.652	0.124
2	LD-PVC	1.6	2.592~2.698	0.106
	PTFE	2.06	2.585~2.695	0.110
	PMMA	2.6	2.554~2.673	0.119
	PC	2.8	2.522~2.648	0.126



(**a**) (**b**)

Figure 3. Transmission loss for air, and the four tested materials for Position 1 (**a**) and Position 2 (**b**) with the two peaks at f_l and f_h, and ε_r highlighted.

A comparison between simulation results and experimental calibration shows that LD-PVC exhibits the highest discrepancy—up to 1.3% in Position 1 and 2.5% in Position 2. For all other materials, however, the error remains consistently below 1% and 1.5%, respectively, demonstrating good agreement between modeled and measured data and confirming the reliability of the calibration procedure.

4.3. Wood Sample Results

This section reports the resonance behavior of the three wood species (fir, poplar, and beech) measured at Position 1 and Position 2 across ten moisture levels. For all species and configurations, both resonance modes (f_l and f_h) showed a monotonic downward shift as moisture content increased, which is consistent with the rise in effective permittivity and

dielectric losses. The magnitude and linearity of these shifts, however, varied significantly between positions and species, providing insight into the interaction mechanisms between the resonator fields and different wood structures.

Figure 4a shows that f_l and f_h shift, for fir sample, progressively downward with increasing θ (0–5.1%). At θ = 0%, the frequencies were f_l = 2.592 GHz and f_h = 2.699 GHz, aligning with calibration results. Over the full moisture range, f_l decreased by f_l ≈18 MHz and f_h by ≈8.2 MHz. The transmission amplitude |S21| also decreased (≈5 dB for f_l and 1.6 dB for f_h), reflecting moisture-induced dielectric losses. Measurements were stable and showed no anomalies. The low-frequency mode exhibited the highest sensitivity (≈3.5 MHz/%) and the best linearity, confirming its suitability as a primary calibration parameter.

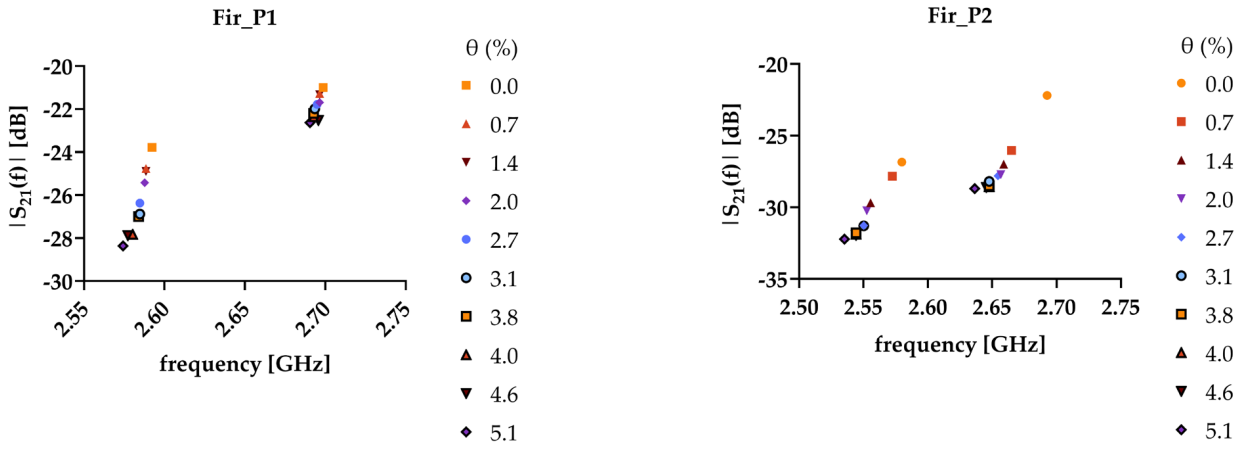


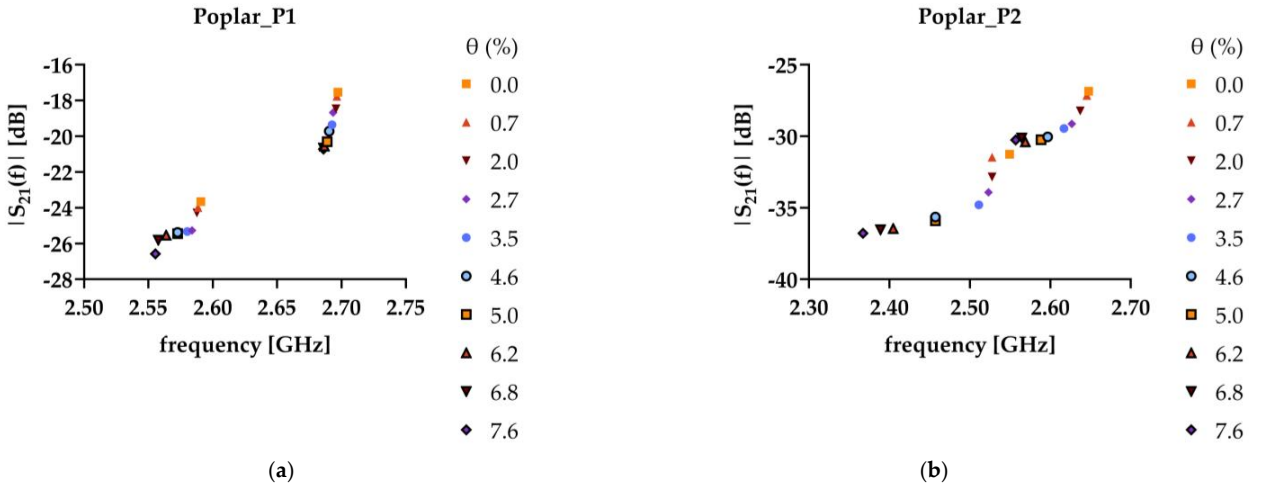
Figure 4. Transmission loss for fir measured at Position 1 (**a**) and Position 2 (**b**) across ten different moisture levels, showing the low- and high-frequency resonant peaks (f_l and f_h).

In Position 2 (Figure 4b), the resonator showed a much stronger response. f_l shifted by −44.5 MHz and f_h by −56.3 MHz, which was more than double the shifts in Position 1. |S21| reductions were also more pronounced. A mild plateau between 2.7% and 4.6% moisture was observed, but both modes remained strictly monotonic. Regression parameters (Table 6) corroborate the enhanced sensitivity of Position 2 (f_l: −7.55 MHz/%, f_h: −8.16 MHz/%), while Position 1 retains slightly higher stability.

Table 6. Linear regression parameters for fir samples measured in Position 1 and Position 2.

Position	Mode	Slope (MHz/%)	Intercept (GHz)	R^2
P1	fl	−3.12	2.59	0.90
	fh	−1.21	2.70	0.71
P2	fl	−7.55	2.57	0.89
	fh	−8.16	2.68	0.81

Figure 5a reports the evolution of the resonance peaks along ten measurement steps for the poplar sample. At the first point, f_l = 2.5907 GHz and f_h = 2.6973 GHz. As the effective moisture perturbation increased, f_l shifted downward by ≈35 MHz, while f_h exhibited a smaller change (~1.6 MHz/step). The transmission amplitude decreased consistently for both modes. The response was repeatable, with no inversions, and f_l remained the most sensitive mode, matching the behavior observed in fir. Position 2 (Figure 5b) again produced larger shifts: −44.5 MHz for f_l and −56.3 MHz for f_h. A shallow plateau at intermediate steps was observed, possibly due to local inhomogeneities, but the global trend remained linear enough for calibration.



(**a**) (**b**)

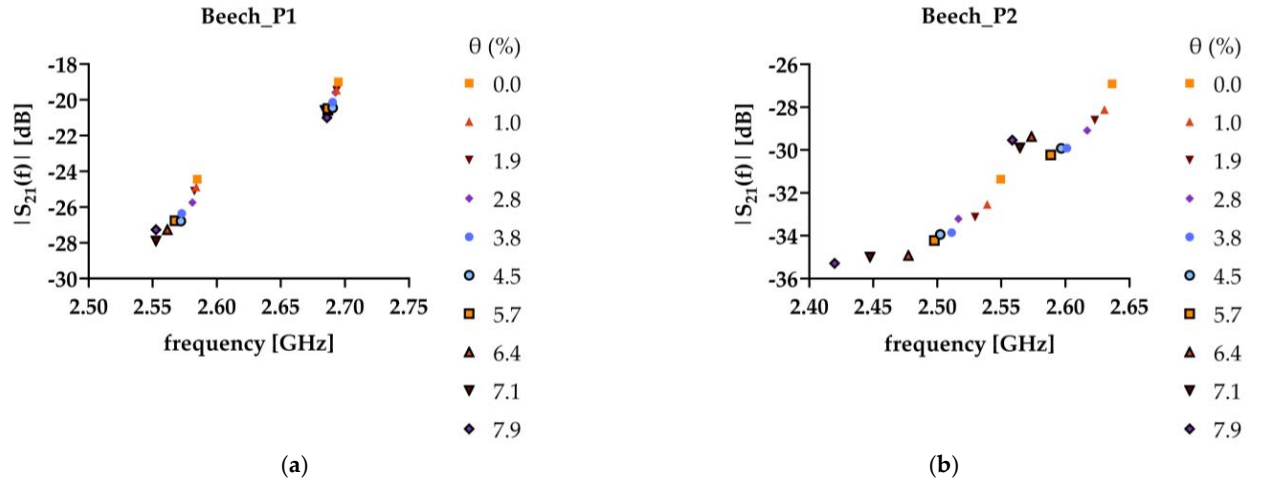
Figure 5. Transmission loss for poplar measured at Position 1 (**a**) and Position 2 (**b**) across ten different moisture levels, showing the low- and high-frequency resonant peaks (fl and fh).

Regression parameters (Table 7) show higher sensitivity for Position 2, while Position 1 maintains excellent linearity, especially for f_l (R^2 = 0.92).

Table 7. Linear regression parameters for poplar samples measured in Position 1 and Position 2.

Position	Mode	Slope (MHz/%)	Intercept (GHz)	R^2
P1	f_l	−4.30	2.59	0.92
	f_h	−2.05	2.70	0.88
P2	f_l	−7.60	2.57	0.87
	f_h	−8.15	2.68	0.85

The behavior of beech (Figure 6a) followed the same general trend but with slightly smaller shifts. At the first point, f_l = 2.5848 GHz and f_h = 2.6950 GHz. Over the ten steps, f_l decreased by ≈32 MHz, whereas f_h shifted by ≈1.0 MHz/step. Transmission losses increased moderately, which was consistent with progressive dielectric loading. Again, f_l offered the best compromise between sensitivity (≈3.2 MHz/step) and linearity (R^2 = 0.91).



(**a**) (**b**)

Figure 6. Transmission loss for beech measured at Position 1 (**a**) and Position 2 (**b**) across ten different moisture levels, showing the low- and high-frequency resonant peaks (fl and fh).

Position 2 (Figure 6b) produced the largest absolute shifts among all species: f_l decreased by −216.7 MHz and f_h by −210.7 MHz. This strong response reflects the higher

permittivity and density of beech, which interact more strongly with the concentrated fields in the ring gap area.

Linearity remained good (Table 8), though steeper slopes imply a higher susceptibility to measurement noise.

Table 8. Linear regression parameters for beech samples measured in Position 1 and Position 2.

Position	Mode	Slope (MHz/%)	Intercept (GHz)	R^2
P1	*fl*	−3.35	2.585	0.91
	fh	−0.95	2.693	0.85
P2	*fl*	−9.00	2.637	0.88
	fh	−6.85	2.630	0.86

At 0% moisture, beech was also measured along axial (A), transversal (B), and radial (C) directions (Figure 7).

- Position 1: resonance frequencies differed only slightly across directions (variations < 2 MHz), indicating quasi-isotropic behavior for this configuration.
- Position 2: differences were more pronounced (e.g., f_l ranged from 2.5023 to 2.5195 GHz), reflecting the stronger field–material interaction in the gap region and increased sensitivity to anisotropy.

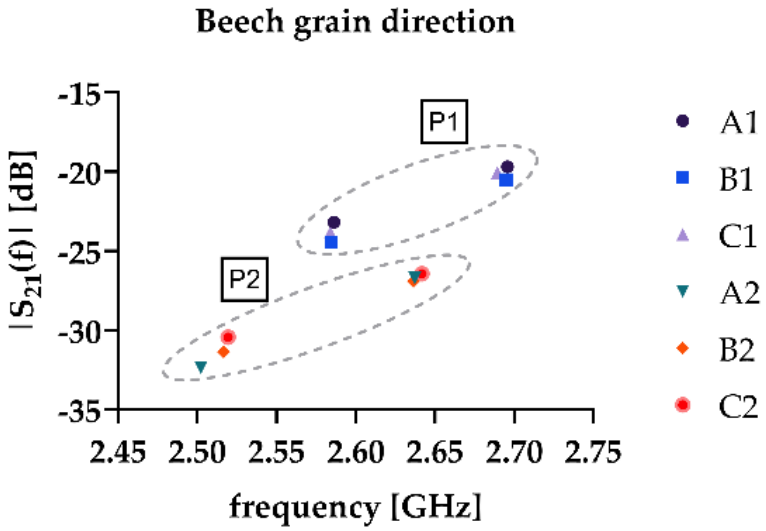


Figure 7. Resonant frequencies and transmission amplitudes for beech at 0% moisture content measured along three grain directions (A, B, and C) for P1 and P2.

This confirms that Position 1 is more suitable for repeatable, direction-independent measurements, whereas Position 2 enhances interaction with the wood's microstructure.

Position 2 exhibits higher sensitivity to moisture variations but also a stronger dependence on the wood grain orientation. This behavior can be conceptually explained by the distribution of the electromagnetic field in the ring resonator. At Position 2, the field is concentrated near the gap region, resulting in a localized interaction with the wood sample. Local variations in density, fiber direction, or microstructure therefore produce measurable perturbations in the resonant frequency. In contrast, Position 1 interacts more uniformly with the sample, averaging out anisotropic effects and providing a quasi-isotropic response. This conceptual model is consistent with the observed linearity and sensitivity patterns across the three wood species, highlighting how field localization can enhance sensitivity while increasing susceptibility to microstructural heterogeneities.

Based on the measured sensitivities of the resonant modes (typically 3–9 MHz/% depending on species and measurement position), the instrumental frequency uncertainty of $U_f = 1.12$ MHz translates into the following moisture uncertainty, defined in Equation (11):

$$U_\theta \approx \frac{U_f}{S_f} \approx 0.12\% - 0.35\% \quad (11)$$

This uncertainty represents a lower-bound estimate under controlled laboratory conditions, as it accounts only for instrumental contributions and does not include additional sources related to sample heterogeneity or positioning. Moreover, the uncertainty range is significantly smaller than the moisture variations investigated in this study and confirms that the resonance-frequency shifts are sufficiently large to ensure reliable moisture estimation even in the low-moisture regime relevant to cultural heritage applications.

The calibration parameters of the adopted model in Equation (9) were derived from the measured sensitivities of the two resonant modes. Finally, Table 9 summarizes the values of α, β and γ for all species and measurement positions. As expected, the low-frequency mode provides the dominant contribution across all species, while the high-frequency mode becomes significantly informative in Position 2, where the field perturbation is stronger. The intercept term γ was consistently negligible ($|\gamma| < 0.02\%$), confirming that dry-state normalization effectively removes systematic offsets.

Table 9. Calibration coefficients for the resonant-frequency moisture model for all species and measurement positions.

Species	Pos	α (*fl*)	β (*fh*)	γ
Fir	P1	−0.321	−0.826	≈0
	P2	−0.132	−0.122	≈0
Poplar	P1	−0.233	−0.488	≈0
	P2	−0.132	−0.123	≈0
Beech	P1	−0.299	−1.053	≈0

From a practical standpoint, the low-frequency mode alone (α term) can be employed when a stable, bulk-averaged estimation of moisture content is required and anisotropic or microstructural effects are negligible, as in quasi-isotropic configurations or for large samples. Conversely, the inclusion of the high-frequency mode (β term) becomes advantageous when enhanced sensitivity to localized dielectric variations or material heterogeneities is desired, as observed in measurements performed under highly localized field configurations (e.g., Position 2). The dual-mode calibration approach therefore provides a flexible framework that can be adapted to different measurement conditions, enabling either a single-mode or combined-mode implementation depending on the desired trade-off between stability and sensitivity.

The comparison reported in Table 10 is intended to provide a qualitative positioning of the proposed sensor within the landscape of existing moisture measurement techniques rather than a direct metrological equivalence, as operating conditions, sensing volumes, and calibration procedures differ across methods For instance, low-frequency capacitive probes achieve accuracies around <2% in permittivity-based moisture estimation, while commercial capacitive moisture meters often report resolutions of ≈0.2–1% for wood materials. In contrast, resistive meter performance varies with species, contact, and environmental conditions.

Table 10. Comparison of moisture measurement methods for wood.

Method or Sensor	Principle	Typical Resolution/ Accuracy	Invasiveness	Measurement Depth/Volume	Notes	References
MPCCRR	Dual-mode resonator (RF resonance)	~0.12–0.35% MC	Non-invasive	Near-surface/ bulk perturbation	Dual-frequency modes capture bulk and localized effects with high sensitivity	This work
Commercial capacitive moisture meters	Capacitive dielectric measurement	≈0.2–1% typical	Non-invasive	Surface/ near-surface	Requires firm surface contact; readings depend on density/species	[32]
Commercial resistance meters (pin)	Electrical resistance/ conductivity	Variable, often ~few %	Invasive (pins)	Between pins only	Dependent on pin contact and wood orientation	[32]
Low-frequency custom capacitive probes	Capacitive permittivity	~<2% error reported	Non-invasive	Surface/ near-surface	Low-frequency dielectric probe for oak and poplar	[33]
ECT capacitance tomography	Electrical capacitance + tomography	RMSEP ~14–24% (wood chips)	Non-invasive	Bulk (tomographic volume)	Focused on wood chip flow MC, large volumes	[34]

A final consideration concerns the limitations of the proposed sensor. In particular, the major limitation is that only small, uniform, laboratory-prepared wood samples were used. While this ensures repeatability, it does not fully capture the variability of cultural heritage materials, such as aged or treated woods, surface roughness, coatings, varnishes, or polychromies. It is important to underline, however, that for painted artifacts, measurements are typically performed on the reverse or in protected areas, reducing the potential interference from surface treatments.

5. Conclusions

This paper presented the calibration of a capacitively coupled ring resonator sensor for the non-invasive measurement of moisture content in wood. Preliminary simulations and reference material tests demonstrated the device's ability to resolve even small variations in permittivity, which is a key requirement for its application to real wood samples. Measurements on three wood species showed a monotonic downward shift in resonant frequencies with increasing water content with Position 2 consistently providing higher sensitivity due to stronger electromagnetic field coupling. Linear regression results confirmed high correlations (typically $R^2 > 0.85$), validating the repeatability and reliability of the method even in the low-moisture regime typical of cultural heritage applications.

The analysis of grain orientation revealed that Position 1 offers a nearly isotropic response, making it suitable for stable baseline measurements, while Position 2 is more affected by fiber direction, providing additional sensitivity to the anisotropic structure of wood. For in situ measurements on cultural heritage artifacts, the orientation of wood fibers is often unknown or cannot be directly accessed. The observed behavior suggests that using Position 1 provides more reliable moisture readings in such cases, as its quasi-isotropic response minimizes errors due to unknown grain direction. Position 2, while more sensitive, should be used when higher resolution is needed or when the local fiber orientation is known or can be reasonably estimated. Combining measurements from both positions could allow practitioners to capture both the bulk moisture content and localized variations related to anisotropy, providing a more complete characterization without invasive sampling.

Overall, the MPCCRR resonator proves to be a compact, sensitive, and fully non-destructive system suitable for monitoring moisture in wooden cultural heritage objects. Its performance suggests strong potential for integration into portable, in situ diagnostic tools for preventive conservation.

While the current uncertainty analysis addresses instrumental contributions, it does not fully propagate uncertainties through the calibration model, particularly those arising from variations in sample geometry and material characteristics. Additionally, only one sample per wood species was tested in this study. While this is sufficient for demonstrating the calibration procedure, it does not capture inter-sample variability, including differences in density, microstructure, or aging conditions.

Future work will extend the experimental campaign to multiple samples per species and will explicitly consider these effects through tests on aged or treated wood samples and under controlled environmental conditions, such as climatic chamber experiments and accelerated aging protocols.

Author Contributions: Conceptualization, L.D. and E.R.; methodology, E.P.; validation, L.D., E.R. and E.P.; formal analysis, E.R.; investigation, L.A.; data curation, E.P.; writing—original draft preparation, L.D. and L.A.; writing—review and editing, Z.D.P. and E.P.; supervision, L.D. and E.R. All authors have read and agreed to the published version of the manuscript.

Funding: This research received no external funding.

Data Availability Statement: The original contributions presented in this study are included in the article. Further inquiries can be directed to the corresponding authors.

Conflicts of Interest: The authors declare no conflicts of interest.

Abbreviations

The following abbreviations and symbols are used in this manuscript, in alphabetic order:

c	Speed of light
ET	Electrical techniques
f_{air}	Air resonant frequency
f_h	High-resonance frequency
f_i	Frequency of the *i-th* sample under test placed on the top of the sensor
f_l	Low-resonance frequency
f_r	Resonance frequency () and its variations
g_f	Feed gaps
g_r	Ring gap
LD-PVC	Low-density polyvinylchloride
L_{eff}	Effective length of the ring
MPCCRR	Microwave Planar Capacitive Coupled Ring Resonator
P1	Position 1
P2	Position 2
PC	Polycarbonate
PMMA	Polymethylmethacrylate
PTFE	Polytetrafluoroethylene
Q	Quality factor
$S(\%)$	The normalized sensitivities
$\lvert S_{21}(f) \rvert$	Transmission scattering parameter
$\lvert S_{ij} \rvert$	Scattering parameters
V	Sample volume and
W_{dry}	Weight of the dried sample
W_i	Weight of the sample at i-th moisture level

Δf	Span between f_h and f_l
ε	Permittivity
ε_{eff}	Effective permittivity of the resonator
ε_r	Relative permittivity
$\theta(\%)$	Gravimetric water content
ρ	Water density

References

1. Hunt, D. Properties of Wood in the Conservation of Historical Wooden Artifacts. *J. Cult. Herit.* **2012**, *13*, S10–S15. [CrossRef]
2. Gjelstrup Björdal, C. Microbial Degradation of Waterlogged Archaeological Wood. *J. Cult. Herit.* **2012**, *13*, S118–S122. [CrossRef]
3. D'Alvia, L.; Palermo, E.; Del Prete, Z. Validation and Application of a Novel Solution for Environmental Monitoring: A Three Months Study at "Minerva Medica" Archaeological Site in Rome. *Measurement* **2018**, *129*, 31–36. [CrossRef]
4. Camuffo, D.; Bertolin, C.; Bonazzi, A.; Campana, F.; Merlo, C. Past, Present and Future Effects of Climate Change on a Wooden Inlay Bookcase Cabinet: A New Methodology Inspired by the Novel European Standard EN 15757:2010. *J. Cult. Herit.* **2014**, *15*, 26–35. [CrossRef]
5. Camuffo, D. Humidity and Deterioration Mechanisms. In *Microclimate for Cultural Heritage*; Elsevier Science: Amsterdam, The Netherlands, 2019.
6. Nilsson, T.; Rowell, R. Historical Wood—Structure and Properties. *J. Cult. Herit.* **2012**, *13*, S5–S9. [CrossRef]
7. Łukomski, M. Painted Wood. What Makes the Paint Crack? *J. Cult. Herit.* **2012**, *13*, S90–S93. [CrossRef]
8. Slávik, R.; Čekon, M.; Štefaňák, J. A Nondestructive Indirect Approach to Long-Term Wood Moisture Monitoring Based on Electrical Methods. *Materials* **2019**, *12*, 2373. [CrossRef]
9. Aichholzer, A.; Schuberth, C.; Mayer, H.; Arthaber, H. Microwave Testing of Moist and Oven-Dry Wood to Evaluate Grain Angle, Density, Moisture Content and the Dielectric Constant of Spruce from 8 GHz to 12 GHz. *Eur. J. Wood Wood Prod.* **2018**, *76*, 89–103. [CrossRef]
10. Dietsch, P.; Franke, S.; Franke, B.; Gamper, A.; Winter, S. Methods to Determine Wood Moisture Content and Their Applicability in Monitoring Concepts. *J. Civ. Struct. Health Monit.* **2015**, *5*, 115–127. [CrossRef]
11. Kylili, A.; Fokaides, P.A.; Christou, P.; Kalogirou, S.A. Infrared Thermography (IRT) Applications for Building Diagnostics: A Review. *Appl. Energy* **2014**, *134*, 531–549. [CrossRef]
12. Niemz, P.; Mannes, D. Non-Destructive Testing of Wood and Wood-Based Materials. *J. Cult. Herit.* **2012**, *13*, S26–S34. [CrossRef]
13. Cataldo, A.; Monti, G.; De Benedetto, E.; Cannazza, G.; Tarricone, L. A Noninvasive Resonance-Based Method for Moisture Content Evaluation Through Microstrip Antennas. *IEEE Trans. Instrum. Meas.* **2009**, *58*, 1420–1426. [CrossRef]
14. D'Alvia, L.; Pittella, E.; Rizzuto, E.; Piuzzi, E.; Del Prete, Z. A Portable Low-Cost Reflectometric Setup for Moisture Measurement in Cultural Heritage Masonry Unit. *Measurement* **2022**, *189*, 110438. [CrossRef]
15. D'Alvia, L.; Palermo, E.; Del Prete, Z.; Pittella, E.; Pisa, S.; Piuzzi, E. A Comparative Evaluation of Patch Resonators Layouts for Moisture Measurement in Historic Masonry Units. In Proceedings of the 2019 IMEKO TC4 International Conference on Metrology for Archaeology and Cultural Heritage, Florence, Italy, 4–6 December 2019.
16. Razafindratsima, S.; Sbartaï, Z.M.; Demontoux, F. Permittivity Measurement of Wood Material over a Wide Range of Moisture Content. *Wood Sci. Technol.* **2017**, *51*, 1421–1431. [CrossRef]
17. Kumar, G.; Ray, K.P. *Broadband Microstrip Antenna Array*, 1st ed.; Artech House: Boston, MA, USA; London, UK, 2002.
18. Abdelgwad, A.H. Microstrip Patch Antenna Enhancement Techniques. *Eng. Technol. Int. J. Electron. Commun. Eng.* **2018**, *12*, 703–710.
19. Alahnomi, R.A.; Zakaria, Z.; Yussof, Z.M.; Althuwayb, A.A.; Alhegazi, A.; Alsariera, H.; Rahman, N.A. Review of Recent Microwave Planar Resonator-Based Sensors: Techniques of Complex Permittivity Extraction, Applications, Open Challenges and Future Research Directions. *Sensors* **2021**, *21*, 2267. [CrossRef]
20. Ekmekci, E.; Kose, U.; Cinar, A.; Ertan, O.; Ekmekci, Z. The Use of Metamaterial Type Double-Sided Resonator Structures in Humidity and Concentration Sensing Applications. *Sens. Actuators A Phys.* **2019**, *297*, 111559. [CrossRef]
21. Xie, Y.; Yang, X.; Xiao, H.; Wang, Y. A Split-Ring Resonator Probe for Assessing Subsurface Wood Defects. *Rev. Sci. Instrum.* **2019**, *90*, 125004. [CrossRef]
22. Pittella, E.; Schiavoni, R.; Monti, G.; Masciullo, A.; Scarpetta, M.; Cataldo, A.; Piuzzi, E. Split Ring Resonator Network and Diffused Sensing Element Embedded in a Concrete Beam for Structural Health Monitoring. *Sensors* **2022**, *22*, 6398. [CrossRef]
23. Torgovnikov, G.I. *Dielectric Properties of Wood-Based Materials*; Springer: Berlin/Heidelberg, Germany, 1993; pp. 135–159.
24. Piuzzi, E.; Pittella, E.; Pisa, S.; Cataldo, A.; De Benedetto, E.; Cannazza, G. Microwave Reflectometric Methodologies for Water Content Estimation in Stone-Made Cultural Heritage Materials. *Measurement* **2018**, *118*, 275–281. [CrossRef]

25. D'Alvia, L.; Piuzzi, E.; Cataldo, A.; Del Prete, Z. Permittivity-Based Water Content Calibration Measurement in Wood-Based Cultural Heritage: A Preliminary Study. *Sensors* **2022**, *22*, 2148. [CrossRef]
26. D'alvia, L.; Apa, L.; Rizzuto, E.; Del Prete, Z. Study of Wood Samples Positioning on Two Microwave Planar Coupled Ring Resonators for Water Content Measurements. In Proceedings of the 2023 IMEKO TC-4 International Conference on Metrology for Archaeology and Cultural Heritage, Rome, Italy, 19–21 October 2023.
27. Zarifi, M.H.; Daneshmand, M. Wide Dynamic Range Microwave Planar Coupled Ring Resonator for Sensing Applications. *Appl. Phys. Lett.* **2016**, *108*, 232906. [CrossRef]
28. Waterhouse, R.B. *Microstrip Patch Antennas: A Designer's Guide*; Springer: Boston, MA, USA, 2003; Volume 7.
29. Piuzzi, E.; Cannazza, G.; Cataldo, A.; Chicarella, S.; De Benedetto, E.; Frezza, F.; Pisa, S.; Prontera, S.; Timpani, F. Measurement System for Evaluating Dielectric Permittivity of Granular Materials in the 1.7–2.6-GHz Band. *IEEE Trans. Instrum. Meas.* **2016**, *65*, 1051–1059. [CrossRef]
30. Gibertini Elettronica Srl Load Cell Technical Balance. Available online: https://www.gibertini.com/media/files/cent-2-ita-all-1121-62a5a8ec7eb95480635169.pdf (accessed on 9 October 2023).
31. Pico Technology Ltd. PicoVNA Specifications. Available online: https://www.picotech.com/vector-network-analyzer/picovna/picovna-specifications (accessed on 9 October 2023).
32. Běťák, A.; Zach, J.; Misák, P.; Vaněrek, J. Comparison of Wood Moisture Meters Operating on Different Principles of Measurement. *Buildings* **2023**, *13*, 531. [CrossRef]
33. D'Alvia, L. Low-Frequency Measurement of Moistened Wood-Based Materials. *Metrology* **2025**, *5*, 1. [CrossRef]
34. Pan, P.; McDonald, T.; Fulton, J.; Via, B.; Hung, J. Simultaneous Moisture Content and Mass Flow Measurements in Wood Chip Flows Using Coupled Dielectric and Impact Sensors. *Sensors* **2016**, *17*, 20. [CrossRef]

Disclaimer/Publisher's Note: The statements, opinions and data contained in all publications are solely those of the individual author(s) and contributor(s) and not of MDPI and/or the editor(s). MDPI and/or the editor(s) disclaim responsibility for any injury to people or property resulting from any ideas, methods, instructions or products referred to in the content.